

See discussions, stats, and author profiles for this publication at: <https://www.researchgate.net/publication/51793516>

The Mixing Mechanism during Lithiation of Si Negative Electrode in Li-Ion Batteries: An Ab Initio Molecular Dynamics Study

ARTICLE in NANO LETTERS · NOVEMBER 2011

Impact Factor: 13.59 · DOI: 10.1021/nl203302d · Source: PubMed

CITATIONS

53

READS

108

3 AUTHORS, INCLUDING:



Priya Johari

Brown University

25 PUBLICATIONS 710 CITATIONS

[SEE PROFILE](#)



Yue Qi

Michigan State University

110 PUBLICATIONS 2,485 CITATIONS

[SEE PROFILE](#)

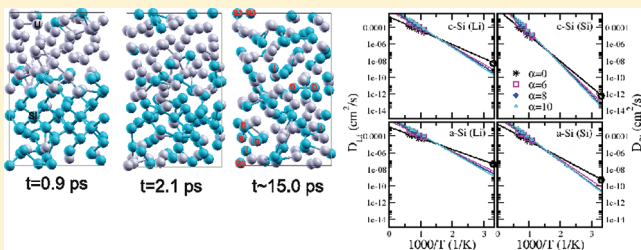
The Mixing Mechanism during Lithiation of Si Negative Electrode in Li-Ion Batteries: An Ab Initio Molecular Dynamics Study

Priya Johari,^{*,†} Yue Qi,^{*,‡} and Vivek B. Shenoy^{*,†}

[†]School of Engineering, Brown University, Providence Rhode Island 02912, United States

[‡]General Motors Global R&D Center, Warren, Michigan 48090, United States

ABSTRACT: In order to realize Si as a negative electrode material in commercial Li-ion batteries, it is important to understand the mixing mechanism of Li and Si, and stress evolution during lithiation in Si negative electrode of Li-ion batteries. Available experiments mainly provide the diffusivity of Li in Si as an averaged property, neglecting information regarding diffusivity of Si. However, if Si can diffuse as fast as Li, the stress generated during Li diffusion can be reduced. We, therefore, studied the diffusivity of Li as well as Si atoms in the Si-anode of Li-ion battery using an ab initio molecular dynamics-based methodology. The electrochemical insertion of Li into crystalline Si prompts a crystalline-to-amorphous phase transition. We considered this situation and thus examined the diffusion kinetics of Li and Si atoms in both crystalline and amorphous Si. We find that Li diffuses faster in amorphous Si as compared to crystalline Si, while Si remains relatively immobile in both cases and generates stresses during lithiation. To further understand the mixing mechanism and to relate the structure with electrochemical mixing, we analyzed the evolution of the structure during lithiation and studied the mechanism of breaking of Si–Si network by Li. We find that Li atoms break the Si rings and chains and create ephemeral structures such as stars and boomerangs, which eventually transform to Si–Si dumbbells and isolated Si atoms in the LiSi phase. Our results are found to be in agreement with the available experimental data and provide insights into the mixing mechanism of Li and Si in Si negative electrode of Li-ion batteries.



KEYWORDS: Li-ion battery, Si anode, density functional theory, molecular dynamics

Advanced energy storage technologies for transportation industries require further improvement of the power, energy density, and durability of Li-ion batteries for use in hybrid electric vehicles (HEV), plug-in HEV (PHEV), and all-electric vehicles (EV). Carbon materials, usually in the form of graphite, are commonly used as the negative electrodes in commercial rechargeable lithium ion batteries. Graphite has a theoretical capacity of 372 mAh/g and is lithiated by Li^+ intercalation process. To meet the high energy goals of high capacity and energy density set forth by the automobile industry for lithium ion batteries, materials that form alloys with lithium and have specific capacities an order of magnitude higher than graphite are being investigated. The high charge capacity (~10 times more than graphite), low discharge potential, cheaper cost, and easy availability of Si has made Si or Si containing composites potential candidates as negative electrode (anode) materials in Li-ion batteries. This high capacity, however, is associated with massive volume (~300%) and structural change during the charging and discharging process, which leads to mechanical fracture, disconnection between the particles, irreversible capacity loss, and thus, limited cycle life.^{1–6} Therefore, to improve the performance characteristics of the Si negative electrode and to develop fault tolerant electrode architectures it is necessary to understand the diffusion kinetics and the stress evolution during lithiation. Several experimental and theoretical studies have been carried out to understand the dynamics of Li in the Si-negative

electrode.^{7–26} Various models at the continuum level have also been employed to study diffusion-induced stresses during lithiation of Si in order to improve the durability of Li-ion batteries.^{27–29} However, the experimentally measured Li diffusivity in Si is an averaged property, and theoretical studies have mostly been restricted to the diffusion of a single Li atom in the crystalline Si,^{11,12,16} while to reach the full capacity of Si electrode the amount of Li that diffuses in and out of Si is 4 times more than the amount of Si. Moreover, the dynamics of lithiation of Si can be further complicated by the crystal-to-amorphous phase transformation, which was only started to be accounted for by Liu et al. in recent Si nanowires in situ lithiation observation and modeling.³⁰ Thus, the details of lithiation process are either unknown or have not been considered in the theoretical studies. For example, if Si can diffuse and mix with Li, the stress generated during Li diffusion can be reduced. Therefore, a quantitative understanding of the fundamental interactions between Li and Si atoms and the diffusion kinetics of both the species in the anode is necessary.

It is well-known that the mixing of Li into Si causes structural changes in the negative electrode. In order to optimize performance it is therefore important to trace these changes in the structure during lithiation, which is unfortunately not possible to

Received: September 21, 2011

Revised: October 27, 2011

monitor in amorphous lithiated silicides using conventional methods like diffraction. Nuclear magnetic resonance (NMR) spectroscopy is however a reliable tool to obtain detailed structural information. Key et al.²⁵ used a combination of *in situ* and *ex situ* NMR spectroscopy to investigate the structure of a working Li-ion battery. Later, they also gave a more detailed picture of crystal-to-amorphous phase transition during the first cycle of lithiation, delithiation, and the amorphous lithiation in the subsequent cycles by using a combination of local structure probes, *ex situ*⁷ Li NMR studies, and pair distribution function analysis.²⁶ They elucidated the formation of distinct amorphous lithiated silicide structures having small clusters of Si which later broke into isolated Si atoms. Their *in situ* NMR studies reveal the mixing dynamics and even identify the changes that are difficult to see using *ex situ* methods, but it is still limited because the NMR signals need to be compared with known LiSi compounds to deconvolute the Li–Si bonding change; the NMR signals are averaged in the sample, so local concentration variation and structural change will be buried in the averaged information.

It would be therefore natural to study the structural changes that occur during lithiation using atomic simulations. The details of mixing during lithiation process of Si and the crystalline-to-amorphous phase transition, which have also not been considered in any of the previous computational work,^{12,13,16} should also be studied. Therefore, in the present work we have performed ab initio molecular-dynamics-based calculations for the LiSi phase with an aim of providing a more realistic picture of inter-mixing kinetics and to track the motion of Li and Si in crystalline as well as amorphous Si anodes. In particular, we have

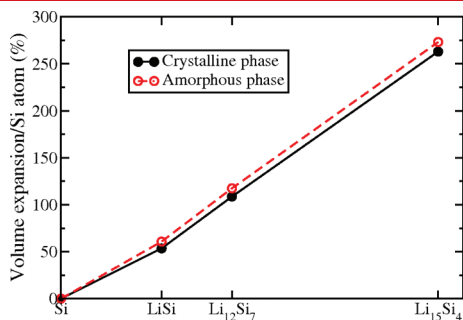


Figure 1. Volume expansion per Si atom for the various crystalline (filled circles) as well as amorphous (empty circles) Li–Si phases.

analyzed the evolution of the structure to elucidate how Li breaks the Si–Si network during the Li–Si mixing process. To this extent we computed the radial distribution functions (RDFs) at various stages of lithiation and analyzed the evolution of Si–Si bonds leading to the formation of rings and other structures. We also computed the diffusivity of both Li and Si at room temperature from first-principles, which to the best of our knowledge has not been computed.

Method. To simulate Li mixing process with Si, we performed ab initio finite temperature molecular dynamics (MD) calculations within the framework of density functional theory (DFT), as implemented in the Vienna Ab Initio Simulation Package (VASP).^{31,32} Projector-augmented-wave (PAW) potentials³³ are used to mimic the ionic cores, while the generalized gradient approximation (GGA) in the Perdew–Burke–Ernzerhof³⁴ (PBE) flavor is employed for the exchange and correlation functional. The optimized coordinates and lattice parameters of c-Si and a-Si were taken from our previous calculations.³⁵ We considered a $2 \times 2 \times 2$ supercell of c-Si and a cubic cell for a-Si,³⁵ both containing 64 Si atoms in all our calculations to keep the same atomic density for all cases. It is well-known that the volume of Si-anode in the Li-ion battery expands on lithiation and this expansion at 0 K is around 60% (50%) for the a-LiSi (c-LiSi) phase (see Figure 1). Therefore, in order to model the LiSi phase we increased the optimized lattice vector of Si³⁵ in z -direction by 60% and filled the space above crystalline and amorphous Si with 64 Li atoms (see Figure 2). The negative heat of formation leads to mixing of Li and Si in the subsequent MD simulations. In Si anodes, a charge transfer step where Li⁺ combines with an electron is required for the formation of Li atoms which then diffuse in the anode. Since electron transport is much faster than the flow of Li⁺ ions in many thin film Si electrode geometries, they combine at the surface of the anode and form Li atoms. Therefore in our current work we focus on the diffusion process of Li atoms in Si. We used a planewave cutoff of 300 eV and a k -point mesh of $2 \times 2 \times 1$ for all calculations. Since the systems considered in the current work are large, we chose a smaller k -mesh. However, before using it for studying diffusion kinetics, we first checked and confirmed that the chosen k -point mesh met standard convergence criteria.

Motivated by experimental work at high temperatures,^{9,14} the MD calculations were performed at temperatures 900, 1050, 1200, 1350, and 1500 K. Starting from the initial configurations shown for $t = 0$ in Figure 2, the cells were allowed to equilibrate at

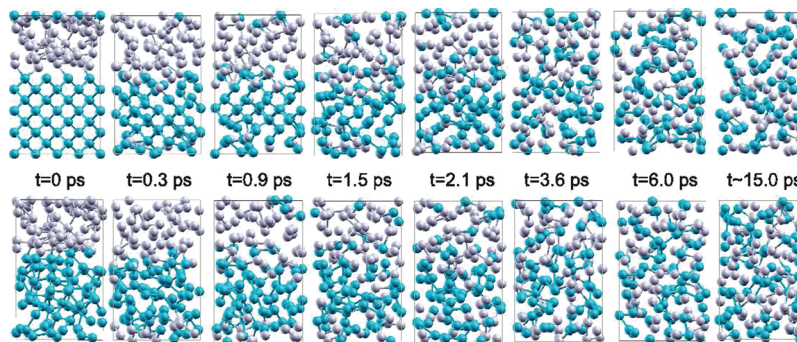


Figure 2. Structures at various stages of lithiation of crystalline (top) as well as amorphous (bottom) Si anode at 1200 K. Structures at $t = 0$ ps and $t \sim 15.0$ ps correspond to the starting and final configurations of our calculations, respectively, while structures at $t = 0.3, 0.9, 1.5, 2.1, 3.6$, and 6.0 ps depict the various intermediate stages of lithiation. In the figure, spheres in cyan and purple color represent Si and Li atoms, respectively.

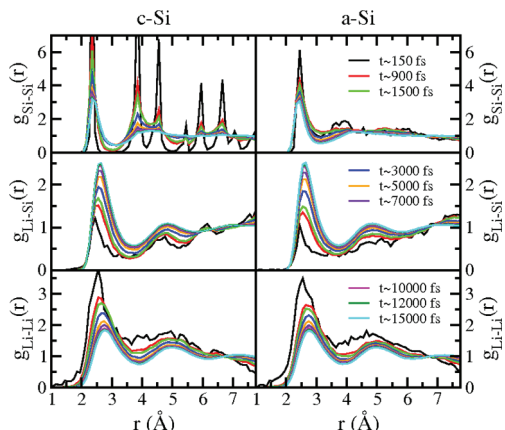


Figure 3. The radial pair distribution function $g(r)$ at 1200 K for Si–Si, Li–Si, and Li–Li pairing in c-Si (left) and a-Si (right) anodes at various stages of lithiation, which is represented here in terms of time steps.

these temperatures for roughly 5000 MD time steps, where each MD step corresponds to 3 fs. This time of approximately 15 ps proved sufficient for substantial mixing of both Li and Si atoms with each other (see Figure 2). In order to check if our results were robust with respect to reduction in the MD time step, we performed a few calculations (not presented here) with an MD time step of 1 fs and found no substantial differences in the results. Moreover, we also found that results presented in our previous work³⁵ corresponding to smaller time step, that is, 1 MD step = 1 fs, are not very different from the results obtained with a larger time step of 3 fs. Mean square displacements (MSD) for Li and Si atoms as function of time were calculated to compute diffusivities at different temperatures. The high-temperature diffusivities were then extrapolated to obtain diffusivities at room temperature.

The evolution of the structure was analyzed by evaluating RDFs (see Figure 3), the size of Si primitive rings (the number of connected Si atoms that form an enclosed ring), and other Si structures during the lithiation process. The ring analysis was performed using the R.I.N.G.S. code,³⁶ while evaluation of the statistics of other structures was carried out using a home-built code. These structures include isolated atoms, dumbbells, boomerangs, and the star structure (see Figure 4), where star is defined as a structure in which an Si atom has 3 or more Si neighbors that have only the Si atom under consideration as their neighbor.

Results and Discussions. Structural Evolution. The starting ($t = 0$ ps), intermediate ($t = 0.3, 0.9, 1.5, 2.1, 3.6,$ and 6.0 ps), and final configurations ($t \sim 15$ ps) of the atoms during intercalation of Li into c-Si (top panel) and a-Si (lower panel) and subsequent equilibration of the a-LiSi phase at 1200 K are shown in Figure 2. It is evident from Figure 2 that the electrochemical insertion of Li atoms into c-Si causes the transformation of crystalline Si to the amorphous phase. Because of the periodic boundary condition, there are Li/Si interfaces in the unit cell. The Li atoms lying near the two interfaces experience a larger driving force to go into Si than the Li atoms sitting in the center of Li cluster and away from the interfaces (see the initial structures corresponding to $t = 0$ ps). The surface Li atoms gradually move inside the Si by breaking the Si–Si bonds and allowing the Si to expand in order to accommodate them. This phenomenon disrupts the structure of the Si anode and creates several local structures during lithiation.

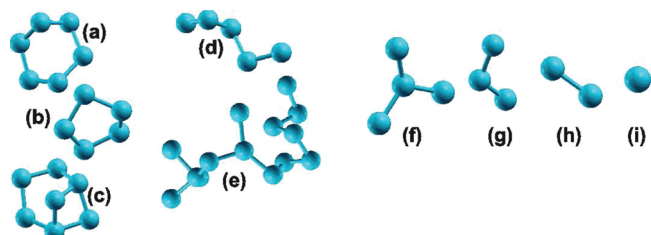


Figure 4. Various structures form during lithiation are presented. Primitive rings of 6 node, 5 node, and 6 and 4 nodes are depicted in (a), (b), and (c), respectively. Other than rings, a few more structures arise, which include (d and e) chains (e.g., a 5 node small chain and a 14 node long chain), (f) stars, (g) boomerangs, (h) dumbbells, and (i) isolated atoms.

In order to understand the evolution of the structure during intercalation, we first studied the RDF, $g(r)$, as a function of time and used the Si–Si bond distance obtained from RDF, to perform an investigation of rings and other structures. Figure 3 shows $g(r)$ for Li–Li, Li–Si, and Si–Si pairs at 1200 K. The left panel of Figure 3 depicts the $g(r)$ for c-Si anode, while the right panel presents it for a-Si. First, Figure 3 demonstrates that with lithiation, the number of Si–Si and Li–Li neighbors decreases, while the number of Li–Si neighbors increases over time, indicating an evaluation of Li–Si mixing process. During the mixing process, we find that in case of c-Si anode, $g_{\text{Si-Si}}(r)$ possesses sharp peaks mainly until $t \sim 3.0$ ps, while at later instances, the second nearest neighbor peak disappears and the remaining peaks become broader, indicating amorphization. The intensity of the peaks also fall with time and becomes almost constant after 3.0 ps, which shows the complete loss of crystallinity, the transformation of crystalline phase into amorphous, and the formation of the amorphous LiSi phase. The resemblance of broad first and second neighbor peaks at around 2.50 and 4.35 Å of the lithiated c-Si with that of the lithiated a-Si features further validates the formation of amorphous structure beyond 3.0 ps. Similar to $g_{\text{Si-Si}}(r)$, we find that after mixing, the $g_{\text{Li-Li}}(r)$ and $g_{\text{Li-Si}}(r)$ graphs of c-Si case match well with the corresponding graphs a-Si. After lithiation, the first neighbor distance is found to be 2.75 Å for Li–Li and 2.5–2.6 Å for Li–Si. We find that there still exists some Si atoms which are covalently bonded, but their bond distance is slightly increased from 2.35 to 2.50 Å after lithiation. This is due to the charge transfer from Li to Si, which causes Si to be negatively charged and develop a repulsive force. The charges in LiSi system can be found with more detailed analysis in refs 11 and 35.

Next, we evaluate the statistics of rings and other structures in order to understand the mechanism of mixing of Li into crystalline and amorphous Si. First, we performed ring statistics analysis for fully optimized c-Si, a-Si, and amorphous LiSi as “sample compounds”. The tetrahedrally bonded c-Si exhibits only 6-atom (node) rings (see Figure 5a). The a-Si contains mainly 5~7 member rings and no rings smaller than 4 nodes, while the mixed LiSi structure has even smaller rings, such as 5 or 3 node rings. The amorphous structures also contain other structures like atomic chains, stars, boomerangs, dumbbells, and isolated Si atoms, which are not ring-structures that can be analyzed by the R.I.N.G code (see Figure 4), but they can be identified by tracking the connected numbers with our home-built code. Li mixing with Si proceeds by breaking the 6-member rings. The top (bottom)-left and top (bottom)-right panels of Figure 6 show

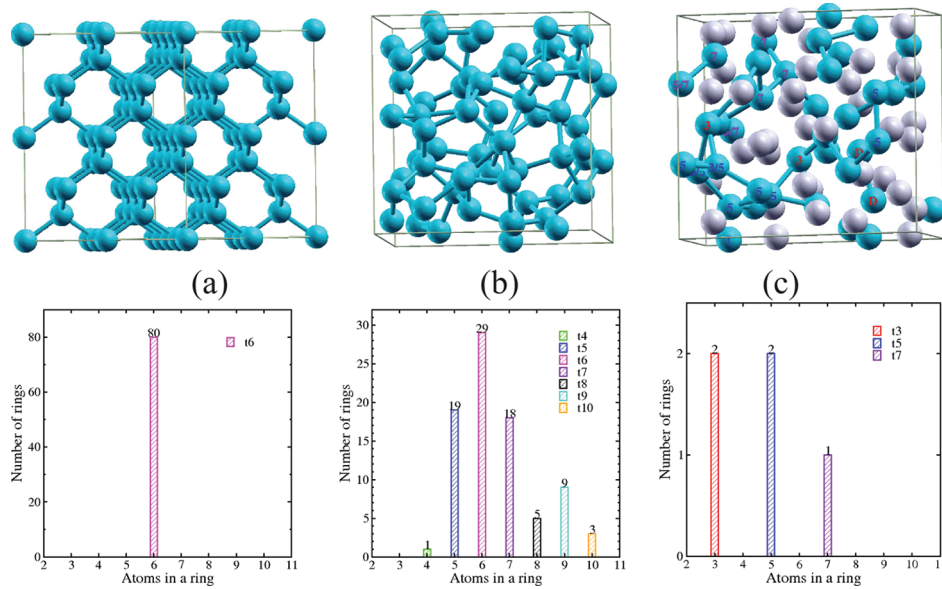


Figure 5. The top panel presents the optimized structures of (a) c-Si, (b) a-Si, and (c) a-LiSi, while the bottom panel depicts their respective rings statistics. The pure Si, in crystalline as well as amorphous form, does not possess any isolated atom, dumbbell, boomerang, or star, while there exists an isolated atom and a dumbbell in the case of a-LiSi. The calculations to study the number of rings and other structures were performed using a cutoff radius of 2.5 Å.

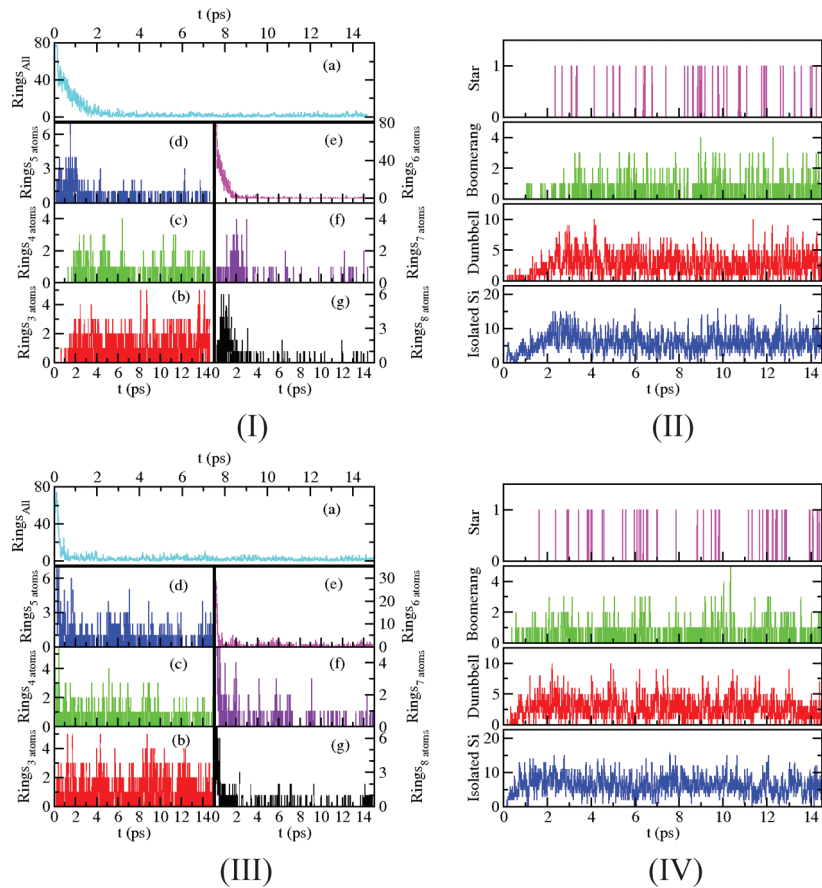


Figure 6. Si rings (left) and other structures such as isolated atoms, dumbbells, boomerangs, and stars (right) statistics with time are presented for the case of c-Si (top) as well as a-Si (bottom), when $T = 1200$ K. The calculations to study the number of rings and other structures were performed using a cutoff radius of 2.5 Å.

the statistics of Si rings and other structures (isolated atoms, dumbbells, boomerangs, and star), respectively, during the lithiation process in c-Si (a-Si) at $T = 1200$ K. It is clear from Figure 6-*Ia* that the total number of rings reduces with time. Comparing the total number of all the rings (*a*) and the number of 6 node rings (*e*) for c-Si in Figure 6, all rings are 6-member rings in crystalline Si before Li mixing. The Li atoms first break the Si–Si bonds of the conventional 6 node rings and create the rings with 5, 7, 8, and even more atoms in the first 2 ps of the simulation, which gradually dissociate into smaller rings of 3, 4, and 5 atoms afterward with the increasing Li concentration.²⁷ The 6 node Si rings diminish completely once Li and Si are fully mixed, while few 7 node rings still exist, which indicates the formation of the a-LiSi phase (see right panel of Figure 5). A similar evolution of rings is seen in the case of a-Si. The total number of rings however reduces more rapidly in the case of a-Si as compared to c-Si, which shows a faster diffusion of Li in a-Si. On analyzing other structures (see the right panel of Figure 6), we see that stars and boomerangs appear occasionally and are temporary, while the number of dumbbells and isolated Si atoms increases with lithiation and stays roughly constant when Li and Si are well mixed ($t \geq 4$ ps). This again confirms the formation of the a-LiSi phase, which basically exhibits Si rings, chains, an isolated Si atom, and a dumbbell in its equilibrium state as shown in right panel of Figure 5. The stars and boomerangs mainly appear when Li breaks the Si atoms chain or ring. These structures eventually convert to dumbbells and isolated atoms when further attacked by Li atoms. The increase in Li concentration will even break the dumbbells and isolate Si atoms from each other. Thus, only isolated Si atoms exist in the system when Si gets fully lithiated to $\text{Li}_{15}\text{Si}_4$ or $\text{Li}_{22}\text{Si}_5$ phase (which were analyzed but not shown in this paper). Our investigation agrees well with the real-time nuclear magnetic resonance studies performed by Key and co-workers,^{25,26} which revealed the formation of Si–Si clusters and isolated Si atoms during the first discharge and the formation of only Si atoms at the end of the discharge in an actual working Li-ion battery. Our results are not only consistent with the findings of Key et al.^{25,26} but also present a detailed mechanism regarding evolution of the local structures during Li–Si mixing. We would, however, like to mention here that the statistics presented in Figure 6 are for high temperature ($T = 1200$ K) when the cell is under compressive strain (see Table 1), and thus the number of rings and other structures may vary slightly for the unstrained cell at room temperature.

Diffusivity of Li and Si. It is apparent from the intermediate structures presented in Figure 2 that Li and Si diffuse faster in a-Si as compared to c-Si anode. In order to determine the diffusivity of Li and Si in Si-anode, we calculate average MSD of Li and Si atoms as a function of MD time steps for different temperatures. The simulation temperatures are chosen such that they are below the melting point of Si. The LiSi phase however converts into liquid phase at these high temperatures but should not significantly affect our results as the short-range order of Li–Si alloy remains unaffected in the liquid state.¹³ The average MSD of Li and Si are given in the left panel of Figure 7 for intercalation into c-Si (top) and a-Si (bottom). Each graph contains data corresponding to different temperatures namely 900 K (black), 1050 K (red), 1200 K (green), 1350 K (blue), and 1500 K (magenta). We see that MSD increases linearly with time. The increase in MSD also occurs with increase in temperature. However, this increase is much slower in the case of Si compared to Li. Furthermore, on comparing MSD of Li and Si for different

Table 1. Average Energy (E_{avg}) and Stress (σ_{avg}) are Tabulated for the Intercalation of Li into Crystalline and Amorphous Si Anodes

| T (K) | c-Si | | | a-Si | | |
|------------|-------------------------------|--------------------------|--------------------------------|-------------------------------|--------------------------|--------------------------------|
| | t_{converge} (ps) | E_{avg} (eV) | σ_{avg} (GPa) | t_{converge} (ps) | E_{avg} (eV) | σ_{avg} (GPa) |
| 900 | 7 | -464 | -1.5 | 7 | -462 | -1.5 |
| 1050 | 5 | -460 | -2.0 | 5 | -458 | -1.9 |
| 1200 | 5 | -454 | -2.3 | 5 | -454 | -2.2 |
| 1350 | 4.5 | -450 | -2.5 | 4.5 | -450 | -2.5 |
| 1500 | 4.5 | -447 | -3.0 | 4.5 | -447 | -3.0 |

starting configurations, it is found that in general, both Li and Si travel faster in a-Si as compared to c-Si, which is understandable as Si in crystalline form is more strongly bound than in the amorphous state.

Using the Einstein relation $\langle r^2 \rangle = 6Dt$ we calculate diffusivities of Li as well as Si for different temperatures and extrapolate the data to obtain the diffusivities at room temperature (300 K). The extrapolation is carried out by following the standard expression for diffusivity, $D = D_0 \exp(E_b/kT)$, where E_b is the energy barrier, k is the Boltzmann constant, and T is the temperature. Plots of diffusivity versus $1000/T$ on a log scale for both Si and Li are given in the right panel of Figure 7.

As mentioned before, the volume is kept constant (at the value of 0 K) throughout the calculations and this generates a compressive strain in the cell at high temperatures. Table 1 presents the approximate convergence time to obtain the a-LiSi phase at different temperatures, corresponding converged average energies and stresses. The data in the Table 1 shows that stress increases with temperature. The system is found to be under compressive stress of roughly 1.5 GPa at 900 K, which increases to approximately 3.0 GPa at 1500 K. The constraint on volume expansion generates stresses at high temperatures and thereby, restricts the atoms to diffuse faster than the usual. Since, the stress in the cell is directly proportional to the temperature (see Table 1), at higher temperatures diffusivity will be significantly underestimated, and therefore smaller variations in diffusivities are obtained in the strained cells (see data in black in the graphs at the right panel of Figure 7). This subsequently gives a smaller slope of the extrapolated curve, which clearly shows that the stress in the system is influencing the estimation of diffusivity at room temperature.

In order to correct the effect of stress to accurately estimate the diffusivities of Li and Si in an unstrained cell, we use the following expression provided by Fahmy and Hurt³⁷

$$D = \frac{D_\sigma}{\exp\left(\frac{\alpha\sigma}{G}\right)} \quad (1)$$

The above expression is evaluated by performing some algebraic manipulations in Doolittle's equation,³⁹ which relates the viscosity of the liquid to the free volume, and the Stoke–Einstein equation,⁴⁰ which gives the relationship between the diffusion coefficient and viscosity. In eq 1, D_σ represents the diffusivity in a strained cell, α is defined as diffusion transfer coefficient whose value is chosen in the range of 6 to 10,^{37,38} σ is stress, and G defines modulus of rigidity. We consider $G = 16.5$ GPa from our previous calculations for a-LiSi.³⁵ Diffusivities at various temperatures and

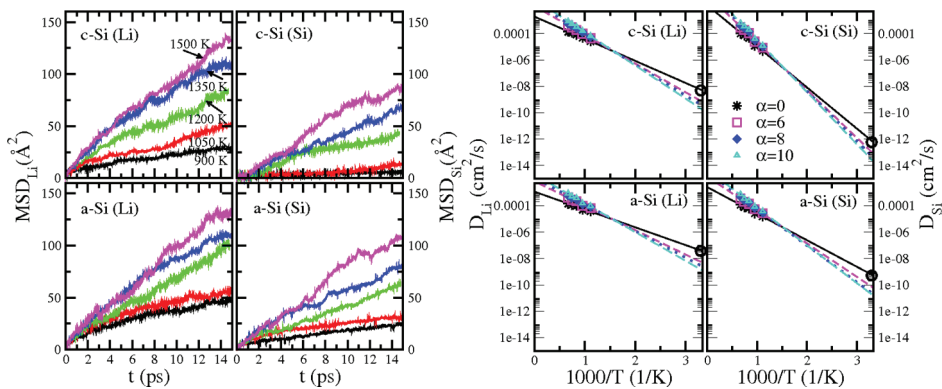


Figure 7. Left panel: Top graphs present MSD of Li and Si in c-Si anode while the bottom graphs show it for the a-Si anode with respect to time for various temperatures such as, 900 K (black), 1050 K (red), 1200 K (green), 1350 K (blue), and 1500 K (magenta). Right panel: Diffusivity of Li (left) and Si (right) in c-Si (top) as well as a-Si anode (bottom) with respect to the inverse of temperature. The value of diffusivity is extrapolated to low temperatures using an exponential fit. Diffusivity in strained cell ($\alpha = 0$) at 300 K is marked by black circle. Diffusivity of Li and Si in unstrained cell is estimated using formula: $D = D_0 / \exp(\alpha\sigma/G)$, where D_0 is the diffusivity under strain, α is diffusion transfer constant whose value is chosen in the range of 6 to 10,^{37,38} σ is stress, and G is modulus of rigidity. Diffusivity at various temperatures, calculated using α equals to 6 (magenta), 8 (blue), and 10 (cyan) are also presented.

Table 2. Computed Diffusion Coefficients and Activation Energy Barriers for c-Si and a-Si at 300 K Based on Different Coupling Parameters

| | $\alpha = 0$ | $\alpha = 6$ | $\alpha = 8$ | $\alpha = 10$ |
|-----------------|------------------------|------------------------|------------------------|------------------------|
| c-Si | | | | |
| D_{Li} | 4.88×10^{-9} | 6.52×10^{-10} | 3.27×10^{-10} | 1.67×10^{-10} |
| D_{Si} | 5.74×10^{-13} | 7.85×10^{-14} | 3.94×10^{-14} | 1.97×10^{-14} |
| D_{Si}/D_{Li} | 1.18×10^{-4} | 1.20×10^{-4} | 1.20×10^{-4} | 1.18×10^{-4} |
| E_b^Li | 0.33 | 0.43 | 0.46 | 0.50 |
| E_b^Si | 0.61 | 0.71 | 0.75 | 0.78 |
| a-Si | | | | |
| D_{Li} | 3.69×10^{-8} | 4.83×10^{-9} | 2.52×10^{-9} | 1.25×10^{-9} |
| D_{Si} | 5.13×10^{-10} | 5.93×10^{-11} | 2.00×10^{-11} | 1.53×10^{-11} |
| D_{Si}/D_{Li} | 1.39×10^{-2} | 1.23×10^{-2} | 0.80×10^{-2} | 1.22×10^{-2} |
| E_b^Li | 0.27 | 0.37 | 0.40 | 0.43 |
| E_b^Si | 0.39 | 0.50 | 0.55 | 0.57 |

stresses corresponding to $\alpha = 6$ (magenta square), 8 (blue diamond), and 10 (cyan triangle) in eq 1 are presented in right panel of Figure 7, while the respective energy barriers and diffusivities at 300 K are tabulated in Table 2.

In a strained cell, without the pressure correction ($\alpha = 0$), the diffusivity of Li and Si in c-Si anode at room temperature is found to be 4.88×10^{-9} and $5.74 \times 10^{-13} \text{ cm}^2 \text{ s}^{-1}$, respectively, while in the case of a-Si anode, we obtain $D_{Li} = 3.69 \times 10^{-8}$ and $D_{Si} = 5.13 \times 10^{-10} \text{ cm}^2 \text{ s}^{-1}$ (see Table 2). These diffusivities lead to an energy barrier of 0.33 and 0.27 eV for Li in c-Si and a-Si, respectively, while the activation energy barrier for Si is found to be 0.61 eV (0.39 eV) in c-Si (a-Si). We note that on applying eq 1, diffusivity of both Li and Si decreases by almost 1–2 orders of magnitude. When $\alpha = 10$, we calculate the diffusivity of Li and Si in c-Si anode at room temperature to be 1.67×10^{-10} and $1.97 \times 10^{-14} \text{ cm}^2 \text{ s}^{-1}$, respectively, while in the case of a-Si, Li and Si diffuse with a rate of 1.25×10^{-9} and $1.53 \times 10^{-11} \text{ cm}^2 \text{ s}^{-1}$, respectively. Our results predict that the diffusivity of Si is 2 orders of magnitude slower than Li in amorphous state and is almost 4 orders of magnitude slower in crystalline Si, which

suggests that Si atoms are relatively stationary during lithiation. If Si atoms are totally immobile, Li has to penetrate the anode by pushing out the Si atoms, resulting in generation of stresses. On the other hand, if Si can diffuse as fast as Li, it can redistribute within the anode to minimize stresses. Gao and his coworkers showed in a recent continuum model that even if the diffusion rate of Si is only 2% of Li, it can still reduce the peak stress generated in Si by 25% comparing to the case without Si diffusion.⁴¹ Therefore, the diffusion of Si in amorphous Si cannot be ignored from continuum level of diffusion-induced stress model. The faster diffusion of Si in amorphous Si helps mitigate the large diffusion-induced stress in Si anode. To the best of our knowledge, the diffusivity of Si in Li_xSi at room temperature has been neither measured nor calculated yet, although a wide range of experimental results are available for the diffusivity of Li in Si. The measured Li diffusivity suggests the value of D_{Li} from 10^{-14} to $10^{-8} \text{ cm}^2 \text{ s}^{-1}$.^{8,9,14,15,18,20} While our results lie well within this range, they are specifically in quite good agreement with the results of Yoshimura et al.¹⁸ and Balke et al.⁹ Yoshimura and his co-workers used bipolar cells and measured diffusivity of Li to be 10^{-9} and $2 \times 10^{-11} \text{ cm}^2 \text{ s}^{-1}$ in vacuum deposited Si film and a single crystal Si plate, respectively,¹⁸ while, Balke et al.⁹ used a diffusivity of around 10^{-8} to $10^{-10} \text{ cm}^2 \text{ s}^{-1}$ to analyze the high-resolution real space mapping of Li-ion transport in a-Si anode in an operational battery.

Conclusions. In summary, we have performed ab initio finite-temperature molecular-dynamics simulations within the framework of density functional theory to study the diffusion kinetics and structure evolution during the lithiation process of crystalline as well as amorphous Si anodes of Li-ion batteries. Li diffuses almost 10 times faster in amorphous than in crystalline Si. We computed Li diffusivity in c-Si and a-Si at room temperature to be in the range of $D_{Li}^{c-Si} = 1.67 \times 10^{-10} \sim 4.88 \times 10^{-9} \text{ cm}^2 \text{ s}^{-1}$ and $D_{Li}^{a-Si} = 1.25 \times 10^{-9} \sim 3.69 \times 10^{-8} \text{ cm}^2 \text{ s}^{-1}$, respectively, depending on the stress and diffusion coupling effect. Our results also reveal that Si is almost immobile as compared to Li and thus, generates stress during lithiation. In order to accommodate Li, the Si atoms move away from their original positions in the process of forming rings, dumbbells, and so forth with a rate in the range of $D_{Si}^{c-Si} = 1.97 \times 10^{-14} \sim 5.74 \times 10^{-13} \text{ cm}^2 \text{ s}^{-1}$ and

$D_{\text{Si}}^{\text{a-Si}} = 1.53 \times 10^{-11} \sim 5.13 \times 10^{-10} \text{ cm}^2 \text{ s}^{-1}$ in c-Si and a-Si, respectively. Note that Si diffuses 1000 times faster in amorphous Si than in crystalline Si, which leads to much easier stress relaxation during lithiation and delithiation. On evaluating the structure evolution during Li mixing with Si, we found that Li atoms break the Si–Si covalent bonds and convert the conventional 6-node-rings into smaller rings and chains and then create temporary structures like stars and boomerangs, which eventually transform to Si–Si dumbbells and isolated Si atoms. These results are found to be in very good agreement with the lithiation process proposed on the basis of NMR experimental observations.

■ AUTHOR INFORMATION

Corresponding Author

*E-mail: (P.J.) Priya_Johari@brown.edu; (Y.Q.) yue.qi@gm.com; (V.B.S.) Vivek_Shenoy@brown.edu.

■ ACKNOWLEDGMENT

The research support of the NSF, the USDOE through the EPSCOR-implementation grant, and the GM-Brown collaborative research laboratory are gratefully acknowledged. Computational support for this research was provided by Grant TG-PHY100022 from the TeraGrid advanced support program and the Center for Computation and Visualization at Brown University. V.B.S. thanks Pradeep Guduru and Vijay Sethuraman for insightful discussions. Y.Q. thanks Min Zhou, Ting Zhu, Xingcheng Xiao, Brian Sheldon, and Mark Verbrugge for stimulating discussions.

■ REFERENCES

- (1) Beaulieu, L. Y.; Hatchard, T. D.; Bonakdarpour, A.; Fleischauer, M. D.; Dahn, J. R. *J. Electrochem. Soc.* **2003**, *150*, A1457–A1464.
- (2) Sharma, R. A.; Seefurth, R. N. *J. Electrochem. Soc.* **1976**, *123*, 1763–1768.
- (3) Wang, W.; Kumta, P. N. *J. Power Sources* **2007**, *172*, 650–658.
- (4) Boukamp, B. A.; Lesh, G. C.; Huggins, R. A. *J. Electrochem. Soc.* **1981**, *128*, 725–729.
- (5) Lee, S. J.; Lee, J. K.; Chung, S. H.; Lee, H. Y.; Lee, S. M.; Baik, H. K. *J. Power Sources* **2001**, *97*–8, 191–193.
- (6) Winter, M.; Besenhard, J. O. *Electrochim. Acta* **1999**, *45*, 31–50.
- (7) Soni, S. K.; Sheldon, B. W.; Xiao, X. C.; Tokranov, A. *Scr. Mater.* **2011**, *64*, 307–310.
- (8) Xie, J.; Imanishi, N.; Zhang, T.; Hirano, A.; Takeda, Y.; Yamamoto, O. *Mater. Chem. Phys.* **2010**, *120*, 421–425.
- (9) Balke, N.; Jesse, S.; Kim, Y.; Adamczyk, L.; Tselev, A.; Ivanov, I. N.; Dudney, N. J.; Kalinin, S. V. *Nano Lett.* **2010**, *10*, 3420–3425.
- (10) Christensen, J. *J. Electrochem. Soc.* **2010**, *157*, A366–A380.
- (11) Chevrier, V. L.; Dahn, J. R. *J. Electrochem. Soc.* **2009**, *156*, A454–A458.
- (12) Kim, H.; Kweon, K. E.; Chou, C. Y.; Ekerdt, J. G.; Hwang, G. S. *J. Phys. Chem. C* **2010**, *114*, 17942–17946.
- (13) Kim, H.; Chou, C. Y.; Ekerdt, J. G.; Hwang, G. S. *J. Phys. Chem. C* **2011**, *115*, 2514–2521.
- (14) Pell, E. M. *Phys. Rev.* **1960**, *119*, 1014–1021.
- (15) Pell, E. M. *Phys. Rev.* **1960**, *119*, 1222–1225.
- (16) Zhang, Q. F.; Zhang, W. X.; Wan, W. H.; Cui, Y.; Wang, E. G. *Nano Lett.* **2010**, *10*, 3243–3249.
- (17) Dewijs, G. A.; Pastore, G.; Selloni, A.; Vanderlugt, W. *Phys. Rev. B* **1993**, *48*, 13459–13468.
- (18) Yoshimura, K.; Suzuki, J.; Sekine, K.; Takamura, T. *J. Power Sources* **2007**, *174*, 653–657.
- (19) Sethuraman, V. A.; Chon, M. J.; Shimshak, M.; Srinivasan, V.; Guduru, P. R. *J. Power Sources* **2010**, *195*, 5062–5066.
- (20) Ding, N.; Xu, J.; Yao, Y. X.; Wegner, G.; Fang, X.; Chen, C. H.; Lieberwirth, I. *Solid State Ionics* **2009**, *180*, 222–225.
- (21) Chan, C. K.; Peng, H. L.; Liu, G.; McIlwrath, K.; Zhang, X. F.; Huggins, R. A.; Cui, Y. *Nat. Nanotechnol.* **2008**, *3*, 31–35.
- (22) Zhao, K. J.; Wang, W. L.; Gregoire, J.; Pharr, M.; Suo, Z. G.; Vlassak, J. J.; Kaxiras, E. *Nano Lett.* **2011**, *11*, 2962–2967.
- (23) Kuhn, A.; Sreeraj, P.; Pottgen, R.; Wiemhofer, H. D.; Wilkening, M.; Heitjans, P. *J. Am. Chem. Soc.* **2011**, *133*, 11018–11021.
- (24) Limthongkul, P.; Jang, Y. I.; Dudney, N. J.; Chiang, Y. M. *Acta Mater.* **2003**, *51*, 1103–1113.
- (25) Key, B.; Bhattacharyya, R.; Morcrette, M.; Seznec, V.; Tarascon, J. M.; Grey, C. P. *J. Am. Chem. Soc.* **2009**, *131*, 9239–9249.
- (26) Key, B.; Morcrette, M.; Tarascon, J. M.; Grey, C. P. *J. Am. Chem. Soc.* **2011**, *133*, 503–512.
- (27) Huang, S.; Zhu, T. *J. Power Sources* **2011**, *196*, 3664–3668.
- (28) Deshpande, R.; Qi, Y.; Cheng, Y. T. *J. Electrochem. Soc.* **2010**, *157*, A967–A971.
- (29) Deshpande, R.; Cheng, Y. T.; Verbrugge, M. W. *J. Power Sources* **2010**, *195*, 5081–5088.
- (30) Liu, X. H. e. a. *Nano Lett.* **2011**, *11*, 3312–3318.
- (31) Kresse, G.; Furthmüller, J. *Phys. Rev. B* **1996**, *54*, 11169–11186.
- (32) Kresse, G.; Furthmüller, J. *Comput. Mater. Sci.* **1996**, *6*, 15–50.
- (33) Kresse, G.; Joubert, D. *Phys. Rev. B* **1999**, *59*, 1758–1775.
- (34) Perdew, J. P.; Burke, K.; Ernzerhof, M. *Phys. Rev. Lett.* **1996**, *77*, 3865–3868.
- (35) Shenoy, V. B.; Johari, P.; Qi, Y. *J. Power Sources* **2010**, *195*, 6825–6830.
- (36) Le Roux, S.; Jund, P. *Comput. Mater. Sci.* **2010**, *49*, 70–83.
- (37) Fahmy, A. A.; Hurt, C. J. *Polym. Compos.* **1980**, *1*, 77–80.
- (38) Shanati, S.; Ellis, N. S.; Randall, T. J.; Marshall, J. M. *Appl. Math. Model.* **1995**, *19*, 87–94.
- (39) Doolittle, A. K. *J. Appl. Phys.* **1951**, *22*, 1031–1035.
- (40) McGregor, R. *Diffusion and Sorption in Fibers and Films*, Vol. 1, Academic Press: New York, 1974.
- (41) Gao, Y. F.; Cho, M.; Zhou, M. submitted to *Journal of the Mechanics and Physics of Solids*.